

ISSN: 2978-0632

Research Article

Open Access Journal of Physics and Science

CoNi/MXene/Cotton Fiber-Based Nonwoven Fabric for Efficient Microwave Absorption

Chunhui Chen^{1,2}, Wei Jiang^{1,2}, Yiqun Fu^{1,2}, Lu Shi³, Qiang Ji^{1,2}, Zhijiang Li^{1,2} and Duo Xu^{1,2*}

¹Xinjiang Production & Construction Corps Key Laboratory of Modern Textile Materials and Technology, Alaer, 843300, China

*Corresponding authors

Duo Xu, Xinjiang Production & Construction Corps Key Laboratory of Modern Textile Materials and Technology, College of Fashion and Textile, Tarim University, Alaer, 843300, China

Received: November 03, 2025; Accepted: November 07, 2025; Published: November 13, 2025

Abstract

The rapid advancement of communication technology, coupled with the increasing severity of electromagnetic pollution, has driven the development of high-performance microwave absorbing materials. In this study, a cotton fiber-based fabric coated with Co-Ni alloy and Ti_3C_2Tx MXene (CFMXSM) was prepared for efficient microwave absorption. Due to the excellent electromagnetic properties of Co-Ni/MXene and the three-dimensional porous structure of the cotton fabric, electromagnetic waves can be attenuated through various mechanisms including dielectric loss, magnetic loss, and multiple reflection loss. By controlling the chemical plating time of Co-Ni and optimizing impedance matching, effective absorption of electromagnetic waves was achieved. With an MXene concentration of 10 mg/ mL, a dipping time of 5 minutes, and a chemical plating time of 15 minutes, the 2.6 mm-thick fabric achieved a reflection loss (RL) of -53.4 dB in the X-band (8.2–12.4 GHz), with an effective absorption bandwidth (RL < -10 dB) covering the entire frequency range. At a thickness of 2.2 mm, the X-band RL reached an excellent value of -64.5 dB. Thus, the fabricated CFMXSM hybrid demonstrates promising potential for applications in the electromagnetic wave protection industry.

Keywords: MXene, Cotton Fiber, Cellulose, Reflection Loss, Microwave Absorption

Introduction

In today's world, marked by the swift development of electronic devices and wireless communication technologies, electromagnetic waves (EMWs) have become an omnipresent phenomenon. While they facilitate human society with numerous conveniences, they simultaneously engender a myriad of issues related to electromagnetic interference (EMI) and environmental pollution [1-4]. As awareness of health and environmental protection intensifies, there is an urgent need to develop electromagnetic wave absorbing materials (EMAMs) that are not only efficient and lightweight but also align with environmentally sustainable [5-7].

Conventional metal-based electromagnetic shielding materials offer high shielding capabilities, however, they are beset by issues such as substantial weight, high costs, and challenging fabrication processes [8,9]. Recently, polymer matrix composites have emerged as a focal point of research within the electromagnetic shielding domain. These composites are lauded for their low density, high corrosion-resistance, and superior workability [10-13]. Notably, cellulose—hailed for its natural, renewable, and biodegradable attributes, coupled with its low density and distinctive microstructure—stands out as an ideal candidate for developing EMAMs [14-16].

MXene is a new type of two-dimensional (2D) transition metal carbide, nitride, and/or carbonitride. The outstanding electrical conductivity of MXene enables the migration of free electrons inside the material when exposed to the action of electromagnetic

Citation: Chunhui Chen, Wei Jiang, Yiqun Fu, Lu Shi, Qiang Ji, et al. CoNi/MXene/Cotton Fiber-Based Nonwoven Fabric for Efficient Microwave Absorption. Open Access J Phys Sci. 2025. 2(4): 1-10. DOI: doi.org/10.61440/OAJPS.2025.v2.19

²College of Fashion and Textile, Tarim University, Alaer, 843300, China

³College of Mechanical Electrification Engineering, Tarim University, Alaer, 843300, China

waves, forming a conduction current. This conduction current converts electromagnetic energy into thermal energy, thereby achieving the absorption of electromagnetic waves. The layered structure of MXene endows it with a large number of interfaces. When electromagnetic waves enter the material, interface polarization occurs between different layers and between the material and the surrounding environment. The charge distribution at the interface is uneven, forming electric dipoles. Under the action of an alternating electromagnetic field, the electric dipoles continuously orient and reverse, thus consuming electromagnetic wave energy. At the same time, the abundant functional groups (-OH, =O, -F, and -Cl) on the surface of MXene will also enhance the interface polarization effect. In addition, multiple reflections and scattering occur inside MXene for electromagnetic waves. This repeated reflection and scattering increases the propagation path of electromagnetic waves in the material, giving electromagnetic waves more opportunities to be absorbed [17,18]. It not only augments the significant electromagnetic loss capability of composite materials but also establishes a robust interfacial bonding with the polymer matrix Through its hydrophilic surface functional groups, thereby enhancing the overall material performance [19, 20]. For example, Tang et al. developed a MXene/cellulose/polyethylene glycol porous composite material revealing an electromagnetic shielding effectiveness (SE) of 60 dB at a thickness of 5 mm [21]. Feng et al. fabricated an MXene/cellulose composite film via a wet co-grinding method, achieving an EMI SE of 36.5 dB at a thickness of 20 µm [22]. However, the enhancement of EMI SE values through improved electrical conductivity of polymer composites leads to increased impedance mismatch, resulting in increased electromagnetic wave reflection which originates the secondary electromagnetic pollution [23-25].

Incorporating magnetic particles into polymeric composite materials can introduce magnetic loss mechanisms [26,27], thereby improving impedance matching and diminishing the reflection of electromagnetic waves (increasing the absorption of EMWs inside the material) [28-31]. Li and colleagues fabricated an MXene-rGO/CoNi film via self-assembly technique, endowed with an abundance of persistent heterogeneous interfaces and reinforced magnetic coupling, which exhibited superior microwave absorption capabilities [32]. The study revealed that rGO/CoNi nanosheets intercalated among MXene layers can act as conductive pathways, ensuring electron migration and an appropriate level of conductive loss capability. Due to the strong magnetic coupling of CoNi alloy nanoparticles on the rGO substrate, the entire MXene-rGO/CoNi film demonstrated significant magnetic loss capability. This structural configuration leverages the synergistic effects of both dielectric and magnetic losses, which is essential for advanced electromagnetic wave absorption materials, manifesting its potential for use in the development of efficient MXene-based microwave absorbers [33]. However, the preparation process of previously prepared magnetic material-doped MXene microwave absorbing materials is relatively complex, the synthesis conditions are relatively challenging, and most of them are formed in the form of films, where the mechanical properties need to be improved.

In this study, a CoNi/MXene/cotton cellulose (CF) nonwoven fabric for electromagnetic wave absorption is reported. The CoNi/MXene/cotton cellulose (CF) nonwoven fabric is prepared

by a simple dipping (MXene) and electroless plating (CoNi) process. The impedance matching and electromagnetic wave attenuation characteristics of the composite fabric are adjusted by controlling the deposition time of CoNi magnetic nanoparticles. The superior electromagnetic properties of CoNi/MXene, combined with the three-dimensional porous structure of cotton cellulose nonwoven fabric, enrich the attenuation mechanism of electromagnetic waves. When the dipping time of MXene is 5 minutes and the deposition time of CoNi nanoparticles is 15 minutes and the thickness is 2.6 mm, the 2.6 mm-thick fabric achieves a reflection loss (RL) of -53.4 dB in the X-band (8.2-12.4 GHz), with an effective absorption bandwidth (RL < -10 dB) covering the entire frequency range. At a thickness of 2.2 mm, the X-band RL reaches an excellent value of -64.5 dB. The wave-absorbing mechanism of the composite fabric is explained in detail. We expect that our work will provide a new way to construct fabric-based wave-absorbing materials.

Experimental Section

Materials

Cotton nonwoven fabric (CF) was purchased from Nangong Saicheng Felt Products Co., Ltd. and preliminarily cut into 5 \times 5 cm patches. Ti $_3$ AlC $_2$ MAX powders (\geq 98% purity) were purchased from Jilin 11 Technology Co., Ltd. Rest of the chemicals including lithium fluoride (LiF), ethanol (C $_2$ H $_5$ OH), hydrochloric acid (HCl), hydrofluoric acid (HF), sodium borohydride (NaBH $_4$, AR), cobalt sulfate heptahydrate (CoSO $_4$ ·7H $_2$ O, AR), nickel sulfate hexahydrate (NiSO $_4$ ·6H $_2$ O, AR), potassium sodium tartrate tetrahydrate (KNa-C $_4$ H $_1$ O $_1$ O, AR), ammonium sulfate ((NH $_4$) $_2$ SO $_4$, AR), and sodium hypophosphite (NaH $_2$ PO $_2$, AR) were obtained from Sigma-Aldrich.

Fabrication of CFMXSM Hybrid

Figure. 1 illustrates the fabrication process of the CFMXSM fabric. The cotton nonwoven fabric (CF) was ultrasonically treated for 5 minutes in ethanol and deionized water solutions to remove excess oil stains and impurities, then dried at 80 °C. The complete procedure of MXene synthesis was followed as reported in reference [30]. The CF was immersed in a 10 mg/mL MXene dispersion, centrifuged at 200 rpm/min for 2 minutes to ensure uniform contact between CF and MXene, then dried at 80 °C to obtain the CFMX sample. The CFMX sample was then immersed in a 0.28 mol/L CoSO₄·7H₂O solution for 20 minutes to adsorb and chelate Co2+ ions, which were then reduced insitu into Co nanoparticles (CoNPs) by a 0.14 mol/L sodium borohydride (NaBH₄) solution, resulting in CFMX-Co0 fabric, whereas any remaining Co²⁺ ions were rinsed off with deionized water. Afterward, a Co-Ni alloy metal layer is grown in-situ around the CoNPs. The Co-Ni electroless plating solution was composed of 2.0 mol/L CoSO₄·7H₂O, 2.0 mol/L NiSO₄·6H₂O, 0.8 M KNaC4H₁₂O₁₀·4H₂O, 0.6 M (NH₄)₂SO₄, and 0.3 M NaH₂PO₂. The pH value of the solution was adjusted to 9.0 with ammonia water, and the temperature was maintained at 80 °C. The electroless plating time varied for 5-, 10-, 15-, and 20-min to obtain samples with different CoNi metal loadings, labeled as CFMXSM-X (X represents the electroless plating time; X = 5, 10, 15, and 20 min).

Characterizations

The fabric samples were conditioned at 20 ± 2 °C and $65 \pm 2\%$ relative humidity for 24 h before various measurements.

Fourier-transform infrared (FT-IR) spectrometer (NicoletIn10MX, Thermo Fisher Scientific, USA) was used for recording IR spectra in diffuse transmittance mode. X-ray photoelectron spectroscopy (XPS) measurement was performed using Escalab instrument (250Xi, Thermo Fisher Scientific, USA) with Mg Kα source radiation to investigate the chemical state and composition of the materials. Surface morphologies and elemental compositions of fabric samples were observed by a field-emission scanning electron microscope (FE-SEM, JSM-7500F, Japan). X-ray diffraction (XRD) patterns were obtained (by a D8 Advance diffractometer, Germany) using Cu $K\alpha$ radiation at a scanning speed of 0.2° min-1 for crystallographic information. Electrical conductivity was measured by a digital multimeter (Keysight 34460, Germany), and magnetic properties were measured by a vibrating sample magnetometer (VSM, Lake Shore 7404, USA) in the field ranging from -20 to 20 kOe.

Electromagnetic Measurement

The electromagnetic properties of the fabric sample were examined using a Vector Network Analyzer (VNA, N5234B, Keysight) using a waveguide method in the X-band frequency range. The electromagnetic properties of the fabric sample were examined using a Vector Network Analyzer (VNA, N5234B, Keysight) using a waveguide method in the X-band frequency range. For the electromagnetic parameter measurement in the X-band (8.2-12.4 GHz) using the Vector Network Analyzer (VNA, Keysight N5234B), the composite fabric samples were precisely cut into rectangular specimens with dimensions of 22.86 mm (length) × 10.16 mm (width) to fit perfectly into the standard WR-90 waveguide. The thickness of the specimen was the natural thickness of the fabric itself, which was measured using a digital thickness gauge at multiple points to ensure consistency. Each specimen was tightly filled into the waveguide cavity to avoid any air gaps that could influence the measurement accuracy.

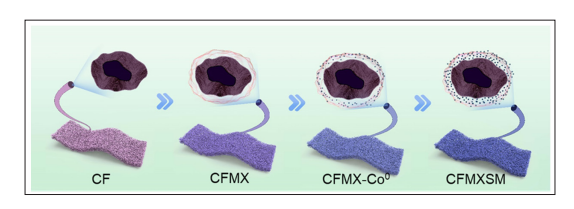


Figure 1: Schematic illustration for the fabrication of CFMXSM hybrid fabrics.

Results and Discussion

Figure. 2a-e and Figure. S1 display the morphological characteristics and three-dimensional porous structures of the cotton nonwoven fabric samples during the processes of CT, MXene infiltration, Co catalytic activation, and CoNi electroless plating. The original cotton nonwoven fabric in Figure. 2a exhibits a smooth surface of individual fibers. After the MXene solution infiltration, MXene flakes adhere to the cotton fibers (Figure. 2b), resulting in a rougher fiber surface due to the noncovalent (e.g., electrostatic adsorption) interactions between the surface functional groups of MXene and cellulose chains, forming a three-dimensional cross-linked network structure binding them together. These rugged surfaces provide a multitude of active sites for Co²⁺ ions attachment, as shown in Figure. 2c where no significant change in fiber morphology is observed

after Co²⁺ ions adsorption. After the in-situ reduction of Co²⁺ ions into Co nanoparticles (CoNPs) using an aqueous solution of NaBH₄, some minute particles can be seen attached to the fibers' surface (Figure. 2d). Following the electroless plating, CoNi nanoparticles are observed to adhere to the fiber surface (Figure. 2f). The EDS elemental mapping images of CFMXSM-15 sample presented in Figure. 2i-j indicate a uniform distribution of Co and Ni elements on the surface, while the presence of O and Ti elements also confirm the successful attachment of 2D MXene nanosheets to the individual fibers.

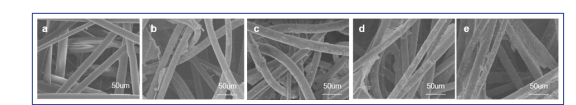


Figure S1: SEM images of (a) CF; (b) CFMX; (c) CFMXSM-Co²⁺; (d) CFMXSM-Co⁰; and (e) CFMXSM-15.

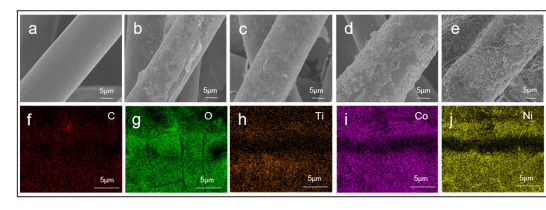


Figure 2: SEM images of (a) CF, (b) CFMX, (c) CFMX- Co²⁺, (d) CFMX-Co0, (e) CFMXSM-15, (f-j) EDS mapping of different elements present in the CFMXSM-15 sample.

Pristine CF fibers and MXene coated fabric were characterized by FTIR for their structural analysis. Figure. 3a presents the FT-IR spectra of CF and CFMX, where CFMX exhibits distinct peaks at 3400 cm⁻¹, 1600 cm⁻¹, and 650 cm⁻¹, corresponding to the γO-H, δH-O-H, and TiO, peaks of MXene [34,35], respectively, confirming the successful attachment of MXene onto the surface of CF. The crystal structures of the pristine CF, CFMX, and CFMXSM-X samples were studied by analyzing their XRD patterns, as shown in Figure. 3b. The first peak of CF at a 20 value of 25.5° is more pronounced, corresponding to the (002) crystal plane of the cellulose fibers. The second weaker peak can be observed at 18.5°, attributed to the (100) plane of the graphitelike structure. The CFMX sample shows a characteristic peak of MXene at an angle of 7.5° [36]. All the CFMXSM-X samples show prominent Bragg reflections at 2θ values of 41.8°, 44.7°, and 47.6°, which are indexed as (1 0 0), (0 0 2), and (1 0 1) planes of hexagonal close-packed (HCP) crystalline phase according to standard diffraction peaks of Co (JCPDS 05-0727) [37]. Singlephase NiNPs exhibit strong diffraction peaks at 44.5°, 51.8°, and 76.4°, corresponding to the (111), (200), and (220) crystal faces of metallic Ni (JCPDS No. 87-712) [38]. It is also evident that in the CFMXSM-X samples, the intensity of Ni peaks increased linearly with increasing the time of electroless plating. XPS spectra were used to further investigate the chemical structure and valence states of different elements in the fabric samples. The XPS survey spectra of pristine CF, CFMX, CFMX-Co2+, CFMX-Co0, and CFMXSM-15 samples are displayed in Figure. 3c. The two principal signals observed at binding energies of 284.6 eV and 532.2 eV are assigned to C 1s and O 1s, respectively, originating from the cellulose content present in the CF sample. The novel peaks that emerge at Ti 2p (456.0 eV) and F 1s (685.0 eV) within the CFMX spectrum confirm the successful adsorption

of MXene flakes, which have fluorine content coming from its surface terminations [39]. Furthermore, the presence of Co 2p (781.2 eV) and Ni 2p (856.2 eV and 873.6 eV) peaks is indicative of the successful catalytic activation by cobalt and the effective electroless plating of CoNi nanoparticles. The further justification for MXene and cellulose adsorption is conducted by deconvolution of C 1s and O 1s signals as shown in Figure. 3d-e. The C 1s corelevel spectrum of CF is deconvoluted into four Gaussian fitting peaks, corresponding to the binding energies of C-C, C-O, C-OH, and O-C=O at 284.9 eV, 286.2 eV, 286.7 eV, and 288.7 eV, respectively. The high-resolution O 1s spectrum is decomposed into three components, representing O-OH, C-O, and C=O, with binding energies of 530.9 eV, 532.1 eV, and 533.2 eV, respectively. Post-MXene infiltration, a redshift of the C-OH C1s peak to 287.2 eV is observed compared to CF, indicating an increase in hydrogen-bonding groups, alongside the emergence of new peaks for C-Ti-O at 282.4 eV and C-Ti at 281.4 eV, corroborating the FT-IR outcomes. The O 1s spectrum of CFMX reveals a novel C-Ti-O peak with a binding energy of 529.5 eV. The Ti 2p XPS spectrum, as shown in Figure. 3f, exhibits characteristic peaks for Ti-C-Tx $2p_{3/2}$ at 455.1 eV, Ti³⁺ $2p_{3/2}$ at 456.4 eV, Ti-O $2p_{3/2}$ at 458.2 eV, Ti^{2+} $2p_{1/2}$ at 461.3 eV, Ti-C-Tx $2p_{1/2}$ at 462.1 eV, and Ti-O 2p_{1/2} at 462.8 eV in CFMX [40]. The core-level spectra of Co 2p obtained from samples before and after in-situ reduction are demonstrated in Figure. 3g-h. Two doublets are separated from the Co 2p scan spectrum of the CFMX-Co²⁺ sample, including divalent cobalt fitting peaks (Co 2p_{3/2} and Co 2p_{1/2}) at 780.8 eV and 796.7 eV and shakeup satellite fitting peaks at 786.2 eV and 802.7 eV. The Co 2p core-level spectrum of the CFMX-Co0 sample is curve-fitted into three doublets: divalent cobalt fitting peaks (Co 2p_{3/2} and Co 2p_{1/2}) at 783.2 and 801.9eV, shakeup satellite fitting peaks at 789.5 and 808.3 eV, and zerovalent cobalt fitting peaks (Co $2p_{3/2}$ and Co $2p_{1/2}$) at 780.7 and 796.7 eV. The generation of zerovalent cobalt species indicates the reduction of segmental Co²⁺ cations to CoNPs [41]. In the high-resolution XPS spectrum of Ni 2p for CFMXSM-15, as depicted in Figure. 3i, two fitting peaks are observed at binding energies of approximately 856.7 eV and 874.7 eV, corresponding to the $2p_{3/2}$ and $2p_{1/2}$ spin-orbit components of metallic nickel (Ni). The deconvoluted peaks, centered at 860.7 eV and 878.5 eV, are indicative of the 2p_{3/2} and 2p_{1/2} spin-orbit components of Ni²⁺, respectively. Furthermore, two satellite peaks, denoted as 'Sat.,' are observed at binding energies of 863.9 eV and 882.2 eV, respectively [42,43].

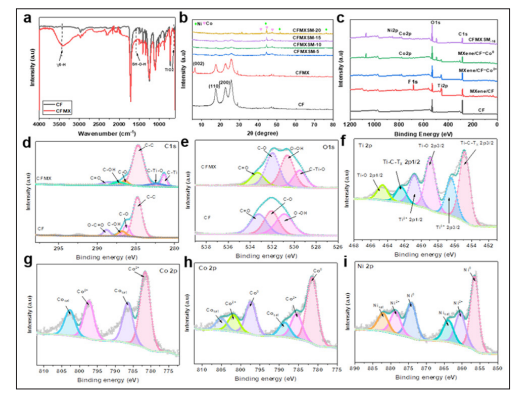


Figure 3: (a) FT-IR spectra of pristine CF and CFMX; (b) XRD patterns of pristine CF, CFMX, and CFMXSM-X samples; (c) XPS survey spectra of pristine CF, CFMX, CFMX-Co²⁺, CF/M-Co⁰ and CFMXSM-15 samples; (d-e) core-level XPS spectra

of C 1s, and O 1s obtained from CF and CFMX samples; (f) core-level XPS spectra of Ti 2p from CFMX samples; (g-h) core-level XPS spectra of Co 2p from CFMX-Co²⁺ and CF/MX-Co⁰⁺ sample; and (i) core-level XPS spectra of Ni 2p from CFMXSM-15 samples.

Figure. 4a demonstrates the changes in the electrical conductivity of CFMXSM-X fabrics as a function of plating time. It's evident that as the electroless plating time increases from 0 min. to 20 min., the electrical conductivity linearly increases from 0.22 S.m-1 to approximately 1438 S.m-1. This enhancement is attributed to the increased deposition of CoNi nanoparticles, which form a conventional conductive network, resulting in a significant increase in the electrical conductivity. Figure. 4b displays the magnetic properties (M-H hysteresis loop) of the CFMXSM-X samples at ambient temperature. The results indicate that as the CoNi content increases, the S-shaped curve demonstrates elevated saturation magnetization (Ms, 21.890 emu/g) and reduced coercivity (Hc, 583.047 Oe), consequently broadening the area of the hysteresis loop. The robust magnetic hysteresis loss of the Co-Ni stratum confers the CFMXSM-X samples with superior magnetic attributes, rendering them suitable for electromagnetic interference (EMI) shielding and absorption applications. The electromagnetic loss capability of electromagnetic wave absorbing materials is commonly assessed by the tangent of the dielectric loss (tan $\delta_a = \epsilon''/\epsilon'$) and the tangent of the magnetic loss $\tan \delta_m = \mu''/\mu'$) [44,45]. The real part ε' , energy storage modulus) and the imaginary part (ε'' , loss modulus) of the complex permittivity ($\epsilon_r = \epsilon' - j\epsilon''$) are instrumental in these calculations. The tangent tanδ values for CFMX and CFMXSM-X, derived from the complex permittivity, are depicted in Figure. 4c and Figure. S2. The dielectric loss components, namely the real part (ϵ ') and the imaginary part (ε'') as well as the tangent of dielectric loss $(\tan \delta)$ demonstrate an increasing trend with extended electroless plating time. For the CFMXSM-X samples, the tano values range from 0.36 to 0.85. Similarly, the real part (μ ', energy storage modulus) and the imaginary part (µ", loss modulus) of the complex permeability $(\mu_r = \mu' - \mu'')$ along with the derived $tan\delta_m$ are illustrated in Figure. 4d and Figure. S3. An increasing trend is observed for the μ' , μ'' and $tan\delta_{m}$ as the electroless plating duration increases, with the $tan\delta_m$ values for CFMXSM-X samples rising from 0.002 to 0.17.

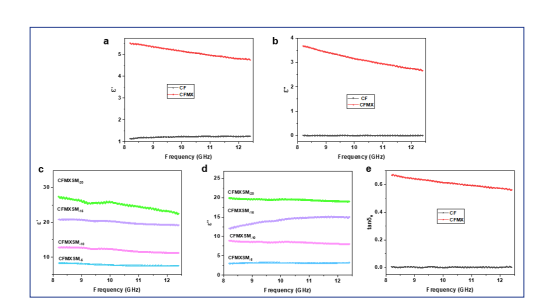


Figure S2: (a-b) ϵ' , ϵ'' of CF and CFMX; (c-d) ϵ' , ϵ'' of CFMXSM-X; and (e) $\tan \delta_e$ of CF and CFMX.

To further explore the dielectric loss mechanisms, Debye theory suggests that the real component (ϵ ') and the imaginary component (ϵ '') of the dielectric constant can be described by the following equations [46].

$$\varepsilon' = \varepsilon_{\infty} + \frac{\varepsilon_s - \varepsilon_{\infty}}{1 + (\omega \tau)^2} \tag{1}$$

$$\varepsilon'' = \frac{\omega \tau(\varepsilon_s - \varepsilon_{\infty})}{1 + (\omega \tau)^2} \tag{2}$$

It can be deduced from equations (1) and (2) that:

$$\varepsilon' - \frac{\varepsilon_s + \varepsilon_\infty}{2} + (\varepsilon'')^2 = \left(\frac{\varepsilon_s + \varepsilon_\infty}{2}\right)^2 \tag{3}$$

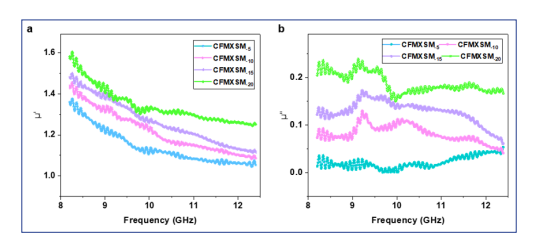


Figure S3: Magnetic parameters including (a) μ^{\wedge} and (b) μ^{\wedge} of CFMXSM-X.

where ω and τ stand for the angular frequency and relaxation time, respectively, ϵ_s and ϵ_∞ represent static permittivity and relative dielectric permittivity for high frequency. Therefore, each semi-circle in the Cole-Cole curves stands for one Debye relaxation process. Figure. 4e-h exhibit the CFMXSM-X with a plethora of Debye dipolar semicircles, signifying the presence of substantial polarization loss.

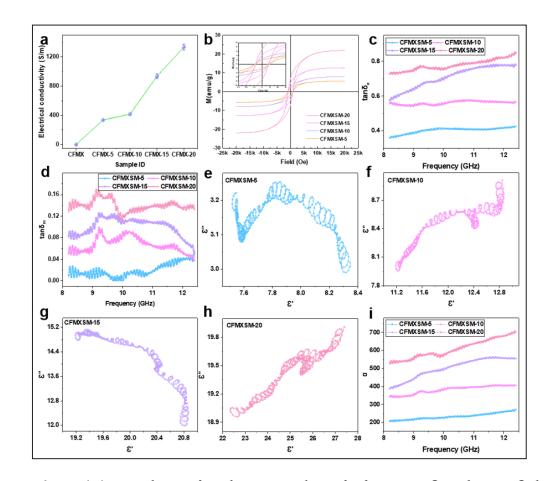


Figure 4: (a) Electrical conductivity of the fabricated CFMXSM-X samples; (b) M–H hysteresis loops of CFMXSM-X samples; (c-d) The $\tan \delta_e$ and $\tan \delta_m$ values of CFMXSM-X samples; (e-h) Cole-Cole plot of CFMXSM-X samples; and (i) attenuation constant αof the CFMXSM-X samples in X-band frequency range.

To gain a deeper understanding of the magnetic loss mechanism, the contribution of eddy current loss was further investigated. According to the skin effect criterion, the eddy current loss can be evaluated by the parameter $C0 = \mu''(\mu') - 2$ f -1. If the magnetic loss stems solely from eddy current effects, the C0 value remains constant over the frequency range. As depicted in Figure. S4, the C0 values for all CFMXSM-X samples exhibit considerable fluctuation throughout the X-band, indicating that eddy current loss is not the dominant contributor. Instead, the observed magnetic loss is primarily attributed to magnetic

resonance processes, including natural resonance and exchange resonance. The well-defined hysteresis loops (Figure. 4b) with appreciable coercivity (Hc) confirm the existence of significant anisotropy energy, which is a prerequisite for natural resonance. Furthermore, the nano-sized dimension and heterogeneous distribution of the CoNi particles could also induce exchange resonance. The synergistic effect between these magnetic resonance mechanisms and the dielectric losses (conduction and polarization) collectively endows the CFMXSM composites with superior electromagnetic wave dissipation capability.

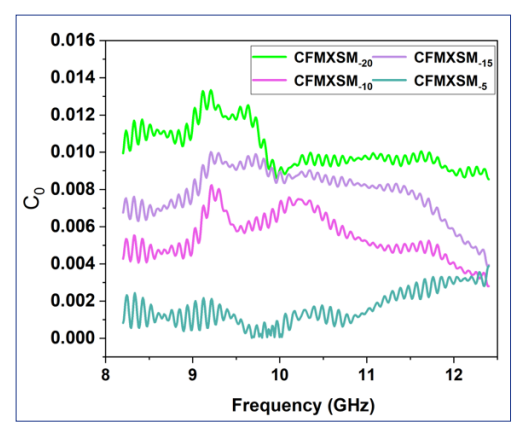


Figure S4: C0_o of of CFMXSM-X.

Attenuation constant α is one of the parameters to measure the overall electromagnetic wave loss capability of the sample, and can be expressed accordingly to electromagnetic wave propagation theory as follows:

$$\alpha = \frac{\sqrt{2\pi} \times \sqrt{(\mu'' \varepsilon'' - \mu' \varepsilon') + \sqrt{(\mu'' \varepsilon'' - \mu' \varepsilon')^2 + (\mu'' \varepsilon'' + \mu' \varepsilon')^2}}}{c}$$
(4)

where f and c represent the frequency and speed of electromagnetic wave, respectively. The α values of the samples, illustrated in Figure. S5 and Figure. 4i, exhibit an increasing trend in correlation with the duration of electroless plating.

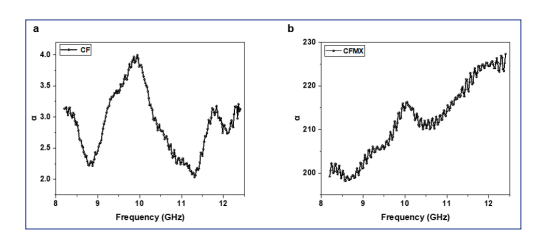


Figure S5: Attenuation constant α of (a) CF and (b) CFMX, respectively.

To gain a deeper understanding of the microwave absorption characteristics of CFMXSM-X composite materials, the reflection loss (RL) values serve as a critical metric for evaluating their performance across diverse applications. The transmission line theory, integral to the analysis and design of high-frequency circuits, provides the theoretical framework for calculating RL values through well-defined equations [47]. This theory is paramount for comprehending and anticipating the behavior of electromagnetic waves along transmission lines, encompassing aspects such as propagation, reflection, and impedance matching. Leveraging the efficacy of the transmission line theory, one can ascertain the reflection loss of microwave absorbent materials

at varying frequencies, which is instrumental in assessing their suitability for different applications [48,49]. For practical applications, an RL value below -10 dB is required, as it ensures the dissipation of at least 90% of the incident EMWs.

$$RL = 20 \log|(Z_{in} - Z_{0})/(Z_{in} + Z_{0})|$$
 (5)

$$Z_{in} = Z_0 \sqrt{\mu_r / \varepsilon_r} \tanh \left[j(2fd/c) \sqrt{\mu_r / \varepsilon_r} \right]$$
 (6)

Where Z_0 and Z_{in} represent the distinctive impedances of the air and absorber surfaces, and d represents the specified thickness ranging from 1 mm to 3.6 mm. As shown in Figure. 5, all the fabricated samples were analyzed for their RL properties measurements. In comparison to CF, both the CFMX and CFMXSM-X exhibit significantly improved RL values, primarily due to the increased electromagnetic attenuation capabilities after the introduction of MXene and CoNi nanoparticles. The RL demonstrates a trend of initial decrease followed by an increase with the increment of thickness. Specifically, CFMX records a minimum RL of -17.0 dB (Figure. 5b), CFMXSM-5 achieves -6.1 dB (Figure. 5c), CFMXSM-10 reaches -7.4 dB (Figure. 5d), CFMXSM-15 attains the most profound RL of -64.5 dB (Figure. 5e), and CFMXSM-20 records -7.1 dB (Figure. 5f). Among these, CFMXSM-15 displays the strongest electromagnetic wave absorption capability. It is observable that the absorption efficacy of the samples does not maintain a direct proportionality to the attenuation constant. The superior microwave absorption performance of materials is intricately linked not only to their inherent wave attenuation capability but also to the impedance matching that facilitates the internal penetration of the incident EMWs to a greater extent along the thickness.

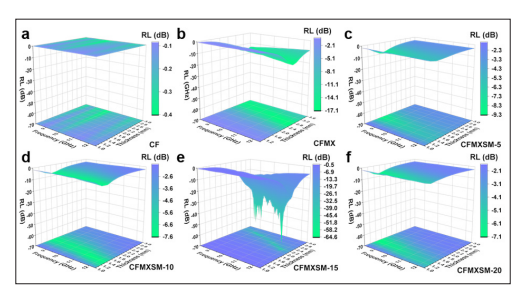


Figure 5: 3D map of reflection loss (RL) of CFMXSM-X samples: (a) CF, (b) CFMX, (c) CFMXSM-5, (d) CFMXSM-10, (e) CFMXSM-15, and (f) CFMXSM-20, respectively.

Impedance matching (Z) represents the ability of a material to capture EMWs and is evaluated by the ratio $Z_{\rm in}/Z_0$. When the Z value is within the range of 0.8–1.2, the impedance of the air is well-matched with that of the absorber. Consequently, the majority of the incident EMWs on the composite material surface can easily penetrate into its interior and dissipate in the form of thermal energy. The RL values and $Z_{\rm in}/Z_0$ values for CFMXSM-15 at a thickness of 1-3.0 mm are shown in Figure. 6 and Figure. S6. As the thickness for CFMXSM-15 samples increases from 1 to 2.0 mm, the RL values decrease, and this trend is also observed with the increase in frequency. When the thickness is within 2.2-2.7 mm, the RL exhibits a minimum value within the X-band and decreases initially then increases with the increase in frequency. The minimum RL (RLmin) shifts to a relatively lower frequency point as the thickness increases.

When the thickness is between 2.8-3.0 mm, the RL values increase with the increase in thickness and also increase at higher frequencies. As shown in Figure. 6b, when the thickness is within 2.2-2.7 mm, the $Z_{\rm in}/Z_0$ values are closer to the range of 0.8–1.2. This is because when the chemical plating time is 15 minutes, the electromagnetic properties constituted by the deposited CoNi nanoparticles, MXene, and CF achieve good impedance matching. At a thickness of 2.2 mm, the RLmin is -64.5 dB, and the effective absorption bandwidth (RL < -10 dB) is 3.0 dB (9.4 to 12.4 GHz). When the thickness is between 2.3-2.6 mm, the absorption bandwidth covers the entire X-band, where the RLmin is -53.4 dB at 2.6 mm thickness.

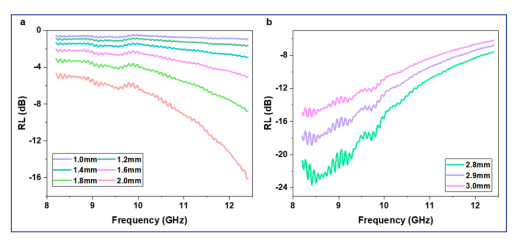


Figure S6: (a-b) RL measurements of CFMXSM-15 composites as a function of frequency of the EMWs.

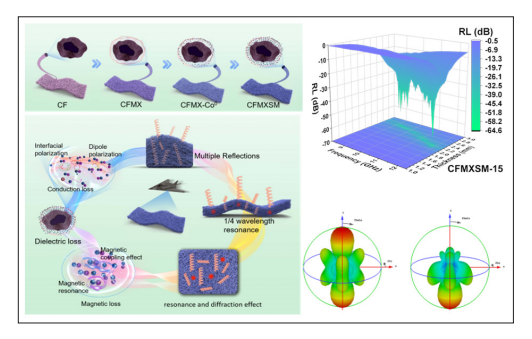


Figure 6: (a) RL measurements and (b) impedance matching of CFMXSM-15 samples of different thicknesses.

To delve deeper into the synergistic relationship between impedance matching and loss capability, a quantitative analysis of the loss mechanisms was conducted. As clearly observed in Figures. 4c and 4d, the dielectric loss tangent (tanδ) for the CFMXSM-15 sample is consistently and significantly greater than its magnetic loss tangent $(\tan \delta_m)$ across the entire X-band. This primary dielectric loss is attributed to the conduction loss from the interconnected MXene network and the strong interfacial polarization at the numerous heterogeneous boundaries. However, the role of magnetic loss is indispensable for achieving the superior absorption performance. The introduced magnetic loss, provided by the CoNi nanoparticles, plays a pivotal role in optimizing the impedance matching. It effectively tailors the electromagnetic parameters, mitigating the impedance barrier that would otherwise result from the excessively high permittivity of a MXene-dominated structure. This function is critical as it enables the efficient entry of incident EMI waves into the absorber. Therefore, a clear synergistic relationship is established: the magnetic component (CoNi) acts primarily as a 'gatekeeper' to facilitate wave penetration by optimizing impedance matching, while the dielectric component (MXene and interfaces) functions as the core 'engine' for energy dissipation. This cooperative effect, operating at the optimal thickness range of 2.2-2.7 mm where both excellent impedance matching (Figure. 6b) and high attenuation capability (Figure. 4i) are achieved, is the fundamental reason

for the outstanding microwave absorption performance of the CFMXSM-15 composite.

To better position the performance of our CFMXSM-15 composite, a comparative analysis with other recently reported microwave absorbers is provided in Table S1. It is evident that our material exhibits highly competitive advantages. The minimum RL value of -64.5 dB at a thickness of 2.2 mm is superior to many advanced absorbers, such as MXene-rGO/CoNi film (-54.1 dB) [32] and MXene@Co hollow spheres (-57.3 dB) [37]. Furthermore, the capability to achieve an effective absorption bandwidth covering the entire X-band at a moderate thickness of 2.6 mm is also remarkable. Beyond the outstanding absorption performance, the unique advantages of our work lie in the utilization of a sustainable, flexible, and low-cost cotton nonwoven fabric as the substrate, and the implementation of a simple, scalable fabrication process. This combination of high performance, flexibility, and sustainability makes the CFMXSM composite a promising candidate for practical electromagnetic wave absorption applications.

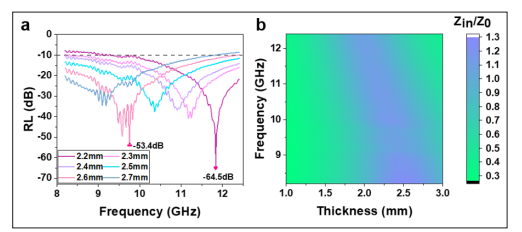


Table of Contents (TOC) Graphic

Figure 7 illustrates the intrinsic mechanism behind EMW absorption by the flexible CFMXSM-X composite fabrics. Upon the incidence of EMWs, the fabric's intricate 3D porous architecture and its tailored electromagnetic properties engender pronounced resonance and scattering phenomena. The stratified integration of CoNi nanoparticles, MXene sheets, and cotton fibers bestows the composite with superior dielectric and magnetic loss attributes, concurrently endowing it with gradient impedance and quarter-wavelength impedance traits [50]. The fabric's structural and electromagnetic characteristics facilitate optimal impedance matching, propelling a substantial influx of EMWs into the material's interior for subsequent attenuation. The non-woven cotton fiber matrix's 3D scaffolding offers an extensive network for electron hopping and a multitude of reflective pathways for

incident EMWs. The MXene component contributes by improving the electrical conductivity, thereby amplifying dielectric losses through conduction and polarization mechanisms. The CoNi nanoparticles, with their robust magnetic properties, account for substantial magnetic losses. These losses originate not only from hysteresis but also from magnetic resonance phenomena (natural and exchange resonance), as confirmed by our analysis of the eddy current effect. The synergistic interface between CoNi nanoparticles and MXene layers stimulates significant interfacial polarization losses [51]. As a result, these attributes render the CFMXSM-X composite fabrics with exceptional capabilities for efficient absorption of electromagnetic waves.

The radar cross section (RCS) serves as a pivotal metric for evaluating the scattering efficiency of a target in response to incident EMWs. Decreasing a target's RCS leads to reduced detectability on radar systems, thereby increasing the concealment (for stealth purposes) and robustness of military hardware. This strategic reduction in RCS is instrumental in advancing the capabilities of military assets by providing a lower probability of intercept and increased operational security. To predict the performance of the CFMXSM-15 radar absorbing material in practical applications, it was overlaid on a perfect electric conductor (PEC), and we utilized CST software to simulate the RCS of the CFMXSM-15 material (Figure 8a). The simulation process involved the use of CST's high-performance 3D EM analysis capabilities, which are designed for the design, analysis, and optimization of electromagnetic components and systems, including the calculation of RCS values. The CFMXSM-15 radar absorbing material, when integrated onto a PEC, exhibits a distinct reduction in radar scattering intensity across a 0-360° range compared to the PEC alone, with a decrease in RCS value of 39.5 dB·m⁻² (Figure 8b-d). Within the X-band frequency range, the RCS of the PEC coated with CFMXSM-15 is consistently lower than that of the uncoated PEC, achieving a significant reduction of 36.1 dB·m⁻² at 10.0 GHz (Figure 8e). This substantial reduction in RCS indicates that the CFMXSM-15 material is highly effective in attenuating the incident EMWs through multiple scatterings, thereby enhancing their absorption within the conductive and magnetic porous structure. These simulation outcomes provide a theoretical foundation for the practical application of CFMXSM-15 in radar absorbing materials, corroborating its potential utility in real-world scenarios.

Table S1. Performance comparison of the CFMXSM-15 absorber with other recently reported microwave absorbing materials.

Absorber Composition	Filler/Matrix Type	Thickness (mm)	Minimum RL (dB)	Effective Bandwidth (GHz)	Ref.
CFMXSM-15 (This work)	Flexible Fabric	2.2	2.2	3.0 (9.4-12.4)	-
		2.6	-53.4	4.2 (8.2-12.4)	-
MXene/CNF/PEG Foam	Porous Foam	3.0	-	(EMI Shielding)	[21]
MXene-rGO/CoNi Film	Flexible Film	2.01	-54.1	3.9	[32]
MXene@Co Hollow Spheres	Powder	2.5	-57.3	3.1	[37]
Fe3O4/C Microspheres	Powder	2.9	-47.8	4.0	[44]

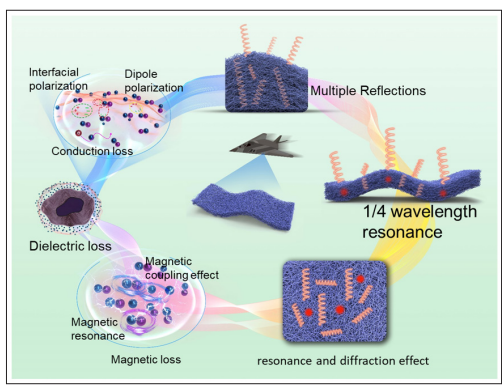


Figure 7: Schematic illustration of the mechanism of electromagnetic wave absorption in CFMXSM-X hybrid fabrics.

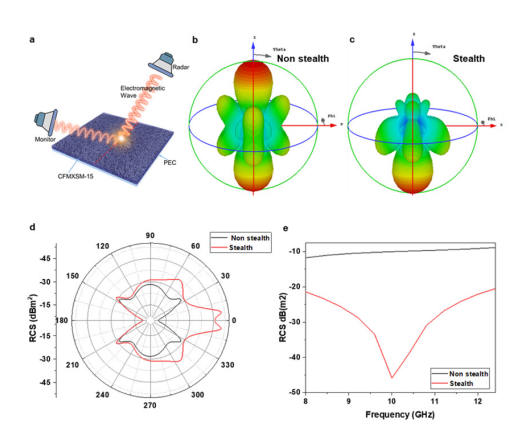


Figure 8: (a) The established micro-satellite model. CST was used to simulate RCS without CFMXSM-15 stealth protection. (b-c) RCS simulation without and with CFMXSM-15 stealth protection. (d) RCS radiation curves within different plane-wave angles at 9.8 GHz. (e) RCS simulation of CFMXSM-15 stealth within X-band (8.2-12.4 GHz) frequency range.

Conclusion

In summary, the CFMXSM-X composite fabric samples, prepared through a simple process of MXene and electroless CoNi deposition, exhibit excellent electromagnetic wave absorption performance. The porous conductive network of the cotton nonwoven fabric provides abundant pathways for EMWs transmission, thereby introducing multiple scatterings of incident waves. By immersing in MXene and adjusting the electroless deposition time, the electromagnetic parameters of the CFMXSM-X samples can be optimized to enhance their wave absorption capabilities. Under the conditions of 10mg/mL MXene concentration, 2 minutes of centrifugation time, and 15 minutes of chemical plating time, the CFMXSM-15 sample with a thickness of 2.6 mm achieves an effective absorption bandwidth (RL < -10 dB) that covers the entire X-band, with an RL value of -53.4 dB. When the thickness is 2.22 mm, the CFMXSM-15 sample reaches a minimum reflection loss (RLmin) of -64.5 dB. The EMW absorbing mechanisms of the CFMXSM-X samples have also been thoroughly investigated, which originate from dielectric loss, magnetic loss, and multiple reflections. These results manifest that CFMXSM-X samples show promising potential for their applications in microwave absorption and other related applications.

Supporting Information

Supporting Information is available from the website.

Acknowledgements

This work was supported by Science and Technology Program of the Production and Construction Corps-Natural Science Support Program-Outstanding Young Talent Program (2025DB006), Open Project of Xinjiang Production & Construction Corps Key Laboratory of Modern Textile Materials and Technology (TDFZKF202404, TDFZKF202403). The President's Youth Fund Project of Tarim University (TDZKSS201915).

Conflict of Interest

The authors declare no conflict of interest.

References

- 1. Lan D, Hu Y, Wang M, Wang Y, Gao ZG, et al. Perspective of electromagnetic wave absorbing materials with continuously tunable effective absorption frequency bands[J]. Compos Commun. 2024. 50: 101993.
- 2. Shi YX, Liang BQ, Gao H, Zhao R, Dong Q, et al. Research progress on spherical carbon-based electromagnetic wave absorbing composites[J]. Carbon 2024: 227: 119244.
- 3. Guler N, Salamah M. Adaptive resource allocation scheme for cooperative transmission in hybrid simultaneous wireless information and power transfer for wireless powered sensor networks[J]. Eng Sci. 2023. 25: 932.
- 4. Cheng J, Li C, Xiong Y, Zhang H, Raza H, et al. Recent advances in design strategies and multifunctionality of flexible electromagnetic interference shielding materials[J]. Nano-Micro Lett. 2022. 14: 80.
- 5. Ruan J, Chang Z, Rong H, Alomar TA, Zhu D, Al Masoud N, et al. High-onductivity nickel shells encapsulated wood-derived porous carbon for improved electromagnetic interference shielding[J]. Carbon. 2023: 213: 118208.
- 6. Chen X, Wu Y, Gu W, Zhou M, Tang S, et al. Research progress on nanostructure design and composition regulation of carbon spheres for the microwave absorption[J]. Carbon. 2022. 189: 617.
- 7. Xu X, Yao F, Abu Ali O, Xie W, Mahmoud SF, et al. Adjustable core-sheath architecture of polyaniline-decorated hollow carbon nanofiber nanocomposites with negative permittivity for superb electromagnetic interference shielding[J]. Adv Compos Hybrid Mater. 2022: 05: 2002.
- 8. Chang JL, Zhai H, Hu ZR, Li JS, Ultra-thin metal composites for electromagnetic interference shielding[J], Compos. Part B Eng. 2022. 246: 110269.
- 9. Cheng Y, Zhu WD, Lu XF, Wang C. One-dimensional metallic, magnetic, and dielectric nanomaterials-based composites for electromagnetic wave interference shielding[J]. Nano Res. 2022. 15: 9595.
- 10. Pang HF, Duan YP, Huang LX, Song LL, Liu J, et al. Research advances in composition, structure and mechanisms of microwave absorbing materials[J]. Compos. Part B Eng. 2021. 224: 109173.
- 11. Dai B, Ma Y, Dong F, Yu J, Ma ML, et al. Overview of MXene and conducting polymer matrix composites for electromagnetic wave absorption. Adv Compos Hybrid Mater. 2022. 05: 704.
- 12. Du B, Zhang DY, Qian JJ, Cai M, He C, et al Multifunctional carbon nanofiber-SiC nanowire aerogel films with superior microwave absorbing performance[J]. Adv Compos Hybrid Mater. 2021. 04: 1281.

- 13. Yu ZH, Yan ZY, Zhang FH, Wang JX, Shao Q, et al. Waterborne acrylic resin co-modified by itaconic acid and γ-methacryloxypropyl triisopropoxidesilane for improved mechanical properties, thermal stability, and corrosion resistance[J]. Prog Org Coat. 2022. 168: 106875.
- 14. Han MR, Zhang RN, Wu QL, Wu N, Liu LR. Biopolymer-Based Aerogels for Electromagnetic Wave Shielding and Absorbing[J]. Chin J Chem. 2022. 417: 129350.
- 15. Liu ZX, Yang HB, Han ZM, Sun WB, Ge XX, et al. A Bioinspired Gradient Design Strategy for Cellulose-Based Electromagnetic Wave Absorbing Structural Materials[J]. Nano Lett. 2024. 24: 881.
- Jiao ZG, Hu JH, Ma ML, Han XK, Ma Y, et al. Research progress of cellulose-derived carbon-based composites for microwave absorption[J]. J Mater Sci Mater Electron. 2023. 34: 536.
- 17. Wang WZ, Cheng HR, Wang JF, Wang SW, Liu XH. Recent Progress and Prospect of MXene-Based Microwave Absorbing Materials[J]. Mater Res Bull. 2024. 179: 112954.
- 18. Du YQ, Yan ZK, You WB, Men QQ, Chen GY, et al. Balancing MXene Surface Termination and Interlayer Spacing Enables Superior Microwave Absorption[J], Adv. Funct. Mater. 2023. 33: 2301449.
- 19. Liu JL, Zhang LM, Wu HJ. Enhancing the Low/Middle-Frequency Electromagnetic Wave Absorption of Metal Sulfides through F- Regulation Engineering[J]. Adv Funct Mater. 2022. 32: 2110496.
- Kabeer N, Vasudevan S, Kaipannan S, Marappan S. Insights into 2D/2D MXene Heterostructures for Improved Synergy in Structure toward Next-Generation Supercapacitors: A Review[J]. Adv Funct Mater. 2022. 32: 2110267.
- Tang JJ, Zuo TC, Feng WQ, Wang W, D Yu, Ti3C2Tx MXene Nanosheet/Cellulose Nanofiber/Poly (ethylene glycol) Porous Composites for Absorption-Dominated Electromagnetic Interference Shielding, ACS Appl. Nano Mater. 2024. 07: 11851.
- 22. Feng SY, Zhan ZY, Yi Y, Zhou ZH, Lu CH. Facile fabrication of MXene/cellulose fiber composite film with homogeneous and aligned structure via wet co-milling for enhancing electromagnetic interference shielding performance, Compos. Part A Appl Sci Manuf. 2022. 157: 106907.
- 23. Liu Y, Liu YJ, Zhao XM, MXene Composite Electromagnetic Shielding Materials: The Latest Research Status. 2024. 16: 41596.
- 24. Wang L, Cheng JW, Zou YX, Zheng WY, Wang YR, et al. Current advances and future perspectives of MXene-based electromagnetic interference shielding materials[J]. Adv Compos Hybrid Mater. 2023. 06: 172.
- Liang CB, Zhang W, Liu CL, He J, Xiang Y, M Han, at el. Multifunctional phase change textiles with electromagnetic interference shielding and multiple thermal response characteristics. Chem Eng J. 2023. 471: 144500.
- 26. Tong SY, Li Y, Ding X, Han RQ, Zhang KY. In situ construction of FeCo nanoparticles decorated nitrogendoped carbon nanofibers with surface-grown carbon nanotubes as lightweight and high-efficiency microwave absorbers with good environmental tolerance. Journal of Environmental Chemical Engineering. 2025. 13: 115141.
- 27. Wu F, Tong SY, Niu J, Xiang Y. Zhou. Ultrathin and lightweight double-layer microwave absorbing coatings based on electrospun FeCo@carbon nanofibers and

- commercial MWCNTs toward highly efficient microwave absorption. Journal of Alloys and Compounds. 2025. 1038: 18281.
- 28. Dong L, Zhou X, Zheng S, Luo Z, Y Nie, et al. Liquid metal@MXene spring supports ionic gel with excellent mechanical properties for high-sensitivity wearable strain sensor[J]. Chem Eng J. 2023. 458: 141370
- 29. Cheng HR, Xing LL, Zuo Y, Pan YM, Huang MN, et al. Constructing nickel chain/MXene networks in melamine foam towards phase change materials for thermal energy management and absorption-dominated electromagnetic interference shielding[J]. Adv Compos Hybrid Mater. 2022. 05: 755.
- Li M, Chen D, Deng XP, Xu BC, Li MY, et al. Graded MXene-doped liquid metal as adhesion interface aiming for conductivity enhancement of hybrid rigid-soft interconnection. ACS Appl Mater Interfaces. 2023. 15: 14948.
- 31. Zhang Y, Meng H, Shi Y, Zhang XF, Liu CX, et al. TiN/Ni/C ternary composites with expanded heterogeneous interfaces for efficient microwave absorption. Compos B Eng. 2020. 193: 108028.
- 32. Li X, Wu ZC, You WB, Yang LT, RC Che. Self-Assembly MXene-rGO/CoNi Film with Massive Continuous Heterointerfaces and Enhanced Magnetic Coupling for Superior Microwave Absorbe. Nano-Micro Lett. 2022. 14: 73.
- 33. Guan GG, Yan L, Zhou YT, Xiang J, Gao GJ, Zhang HY. Composition design and performance regulation of three-dimensional interconnected FeNi@carbon nanofibers as ultra-lightweight and high efficiency electromagnetic wave absorbers. Carbin. 2022. 197: 494.
- 34. Cao WT, Ma C, Tan S, Ma MG, PB Wan. Ultrathin and Flexible CNTs/MXene/Cellulose Nanofibrils Composite Paper for Electromagnetic Interference Shielding. Nano-Micro Lett. 2019. 11: 72.
- 35. Yang YS, Chen KC, Dang BK, Wang C, Chen YP, et al. Flexible and mechanically strong MXene/cellulose-lamellae sheets for electromagnetic interference shielding. Chem Eng J. 2023. 468: 143661.
- Zhou B, Zhang Z, Li YL, Han GJ, Feng YZ, et al. Flexible, Robust, and Multifunctional Electromagnetic Interference Shielding Film with Alternating Cellulose Nanofiber and MXene Layers. ACS Appl Mater Interfaces. 2020. 12: 4895.
- 37. Zhang Y, Liu XH, Guo ZQ, Jia CY, Lu F, et al. MXene@Co hollow spheres structure boosts interfacial polarization for broadband electromagnetic wave absorption. J Mater Sci Technol. 2024. 176: 167.
- 38. Zheng JJ, Li ZH, Zheng JY, Han CC, Chen YM. Heterostructured MXene/Ni Composites for Tunable Electromagnetic Wave Absorption. ACS Appl Nano Mater. 2024. 7: 10860.
- 39. Ma M, Liao XJ, Chu QD, Chen S, Shi YQ. Construction of gradient conductivity cellulose nanofiber/MXene composites with efficient electromagnetic interference shielding and excellent mechanical properties. Compos Sci Technol. 2022, 226, 109540.
- Jia XC, Shen B, Zhang LH, Zheng WG. Construction of compressible polymer/MXene composite foams for high-performance absorption-dominated electromagnetic shielding with ultra-low reflectivity. Carbon. 2021. 173: 932.

- 41. Chen CH, Yu QH, Hai WQ, Shao HQ, Shao GW, et al. Flexible Sandwich-Structured Co–Ni Alloy-Coated Basalt Fabrics via the Writing–Grafting–Activation–Deposition Process for Electromagnetic Interference Shielding and Electrothermal Conversion. ACS Appl Electron Mater. 2022. 04: 6106.
- 42. Xue B, Li Y, Cheng ZL, Yang SD, Xie L, et al. Directional electromagnetic interference shielding based on step-wise asymmetric conductive networks. Nano-Micro Lett. 2022. 14: 16.
- 43. Ma XQ, Chen J, Yuan BF, Li YD, Yu LY, et al. Three-dimensional hollow nickel phosphate microspheres with controllable hoya-like structure for high-performance enzymeless glucose detection and supercapacitor. Appl Surf Sci. 2022. 588: 152928.
- 44. Wang XY, Xing XF, Zhu HS, Li J, Liu T. State of the art and prospects of Fe3O4/carbon microwave absorbing composites from the dimension and structure perspective. Adv Colloid Interface Sci. 2023. 318: 102960.
- 45. Zeng XJ, Cheng XY, Yu RH, Stucky GD. Electromagnetic microwave absorption theory and recent achievements in microwave absorbers. Carbon. 2020. 168: 606.
- 46. Tian W, Li JY, Liu YF, Ali R, Guo Y, et al. Atomic-scale layer-by-layer deposition of FeSiAl@ZnO@Al2O3 hybrid with threshold anti-corrosion and ultra-high microwave absorption properties in low-frequency bands. Nano-Micro Lett. 2021. 13: 161.
- 47. Luo F, Liu DQ, Cao TS, Cheng HF, Kuang JC, et al. Study on broadband microwave absorbing performance of gradient porous structure. Adv Compos Hybrid Mater. 2021. 4: 591.
- 48. Liu B, Li JH, Wang LF, Ren JH, Xu YF. Ultralight graphene aerogel enhanced with transformed micro-structure led by polypyrrole nano-rods and its improved microwave absorption properties, microwave absorption properties. Compos Part A Appl Sci Manuf. 2019. 97: 141.

- 49. Guo Y, Liu H, Wang DD, EI-Bahy ZM, Althakafy JT, et al. Engineering hierarchical heterostructure material based on metal-organic frameworks and cotton fiber for high-efficient microwave absorber. Nano Res. 2022. 15: 6841.
- 50. Li XQ, Guan GG, Tong SY, Chen X, Zhang KY, et al. Multifunctional core–shell CaSnO3@N-doped carbon coaxial nanocables with excellent lithium storage performance and efficient microwave absorption[J]. Inorganic Chemistry Frontiers. 2024. 11: 8392-8410.
- 51. Li XQ, Guan GG, Tong SY, Cheng BJ, Xiang J, et al. Two birds with one stone: Bimetallic ZnCo2S4 polyhedral nanoparticles decorated porous N-doped carbon nanofiber membranes for free-standing flexible anodes and microwave absorption[J]. Journal of Colloid and Interface Science. 2025. 678: 1031-104.